Weldability and mechanical properties of dissimilar laser welded aluminum alloys thin sheets produced by conventional rolling and Additive Manufacturing

Weldability and mechanical properties of dissimilar laser welded aluminum alloys thin sheets produced by conventional rolling and Additive Manufacturing

Vincenzo Dimatteo[a,b], Erica Liverani[a], Alessandro Ascari[a], Alessandro Fortunato[a]

(a) Department of Industrial Engineering (DIN), viale Risorgimento 2, Alma Mater Studiorum - University of Bologna, Bologna (Italy)
(b) Corresponding author: vincenzo.dimatteo4@unibo.it., viale Risorgimento 2, 40136 Bologna, BO, Italy

Abstract

The production of parts involving the combination of different materials has gained a lot of interest in recent years as a strategy for achieving weight reduction. Particular attention has been paid to the joining process of mechanical components obtained with different production processes. This paper aims at studying the feasibility of laser welding to join rolled 6082-T6 thin sheet to A357 sheet produced by Laser-based Powder Bed Fusion (LPBF). The role of welding parameters, LPBF scan strategy and post heat treatment on the weld bead formation has been studied by means of microstructural and mechanical characterization. The results showed that a higher welding speed reduces the porosity in the weld bead obtaining values of about 5% in terms of percentage of fused area, while the post heat treatment of the LPBF sheet has the greatest influence on the final properties of the joint compared to the scanning strategy used. In particular, a complete T6 heat treatment of the additive sheets leads to an ultimate tensile strength of about 200 MPa closes to the reference condition 6082−6082. Hardness measurements showed that a drop in the values occurred at the center of the bead regardless of the treatment conditions while Digital Image Correlation (DIC) strain analysis confirmed that higher deformation occurred in the Fused Zone and in the Heat Affected Zone. SEM-EDS analysis revealed the presence of intergranular precipitates which contain Fe, Si, Mg and Mn in the fused zone.

Keywords

Laser welding, Laser-Based Powder Bed Fusion, Hybrid welding, Digital Imaging Correlation, Microstructure

1. Introduction

In recent years, the reduction of greenhouse gases emissions has become a key point in the legislation of several governments especially in the field of mobility. For example, the European Union (Commision E, 2017) reported that the 12 % of total emission of carbon dioxide (CO_2), the main greenhouse gas, comes from automotive vehicles. To meet these requirements, cars manufacturers are pushing for new technologies especially in the field of electromobility. Saariluoma et al. (2020) showed an overview of the technology's challenges in battery module design and manufacturing, noting that a battery pack for an electric vehicle consists of hundreds of cells connected to each other and a battery case that has both the protective and cooling function. Zwicker et al. (2020) pointed out that due to the large number of cells in a battery pack module and the large number of modules that make up an electric vehicle it is necessary to optimize the efficiency of a module and reduce the weight. Hong and Shin (2017) reported that weight reduction is directly linked to the employment of light alloys, and in this context, aluminum alloys fit well thanks to low production costs and their high strength to weight ratio. The module's weight decreasing and the efficiency improvement of a battery pack through the cooling optimization, could be reached combining different materials and technological processes, as reported by Moller et al. (2020). Structural aluminum parts, usually aluminum 6xxx alloys, are obtained through conventional technologies such as plastic deformation and casting, but these processes suffer in terms of achievable customization and geometric flexibility.

Additive manufacturing (AM) technologies have gained an undoubtable industrial attention thanks to their capability to produce three-dimensional parts with no limits of the shapes and geometries. Among the AM processes, Laser-based Powder Bed Fusion (LPBF), in which the parts are obtained from the metal powder by stacking and melting the powder layer by layer by laser beam, is certainly the most used. Yang et al. (2018) reported that the traditional cast Al-Si-Mg alloys, are the most investigated aluminum alloys in LPBF due to their good castability and mechanical properties. Vilaro et al. (2008) pointed out that thanks to their structural durability and good corrosion resistance, Al-Si-Mg alloys are also demanded for automotive industry. One of the strengths of AM, as mentioned before, is certainly the freedom to design structures characterized by geometries that cannot be obtained with conventional processes. In particular, the use of AM is a promising approach to design conforming cooling channel in order to improve the cooling rate and therefore the module efficiency for example in a Lithium-Ion battery case. Tan et al. (2020) studied the design of novel conformal cooling channels (CCC) molds produced by AM. Holker et al. (2015) demonstrated the feasibility of aluminum hot extrusion dies with CCC produced by LPBF. Despite the advantages in the use of AM, a major drawback is related to the components dimension which are strongly dependents to the size of chamber. In order to overcome this problem a possible way could be join the LPBF complex parts with conventional components. In recent years, several studies have been performed in the field of joining of LPBF components. Prashanth et al. (2017) studied the possibility to exploit the friction stir welding process to weld Ti6Al4V parts; Du et al. (2018) studied the feasibility of friction stir welding on aluminum components produced by LPBF with the aim to reduce the porosity and enhance the mechanical properties. Although good results have been obtained with this technology, it suffers from a lack of flexibility, repeatability and automation and thus not suitable for mass production. In this scenario, laser beam welding (LBM) could be an interesting alternative thanks to

its particular characteristics such as high power focused on a small spot, high welding speed, small deformation of the parts and high flexibility.

Autogenous joining of Al-Si-Mg alloys by means of laser radiation poses several challenges due high reflectivity to the infrared laser beam, low viscosity and the presence of alloy elements resulting in porosity and weld crack formation. Laser beam welding has been successfully applied in joining of hybrid components parts (LPBF parts to conventional rolling sheets) in similar and dissimilar configuration. For example, Ascari et al. (2016) exploited the possibility to apply laser technology to join AISI 316L hot rolled sheets with LPBF components of the same steel, while Yang et al. (2019) investigated the laser weldability of AISI 304 LPBF parts. In both papers interesting results were presented, demonstrating the feasibility of the laser welding process in joining dissimilar components. However, to the author's best knowledge, no researchers have conducted studies on the weldability of Al-Si-Mg parts produced by LPBF and rolling sheets of 6xxx alloys in dissimilar configuration.

In this view, the proposed paper is focused on determine the feasibility of laser technology to join thin sheets in dissimilar configuration. Laser welding jointed a 2 mm thick commercial AlSi1MgMn (designated as 6082-T6) produced by conventional hot rolling process with a 2 mm thick AlSi7Mg0.6 (designated as A357) produced by LPBF. The effects of LPBF process and post-process conditions and the laser welding parameters were studied by mechanical and microstructural point of view. The correlation of the results obtained with all the aforementioned analysis allowed to define an optimized manufacturing process for dissimilar laser welded Al-based alloy.

2. Materials and methods

2.1. LPBF manufacturing and post-processes

A357 atomized powder, supplied by Carpenter (Carpenter Additive, Carpenter Technology Corporation, USA) with the chemical composition reported in Table 1, was used for manufacturing LPBF sheets. The powder was spherical in shape with dimensions in the range of 20-63 µm.

Table 1: Powder chemical composition [wt.%]

Al	*Si*	*Mg*	*Fe*	*Ti*	*Cu*	*Mn*	*N*	*Other*
Balance	6.90	0.55	0.09	0.09	< 0.05	< 0.01	< 0.2	< 0.1

The LPBF parts were produced using a SISMA MYSINT100 system in a building platform of 100 mm in diameter. All samples were built in a nitrogen environment with a residual oxygen content < 0.1 % using the same laser parameters, optimized in previous studies (Tonelli et al., 2020) and summarized in Table 2. Two different building orientations (see Figure 1) were established in order to evaluate the effect of LPBF metallurgical and mechanical anisotropy on weld joint. Each build job was carried out with the same samples number (6 for O-series and 12 for V-series) in order to assure equal in-process condition, for a total of 42 half metal sheet samples with dimensions of 25 mm x 80 mm x 2 mm.

Table 2: LPBF process parameters

Power [W]	**Scan speed [mm/s]**	**Hatch distance [µm]**	**Layer thickness [µm]**	**Scanning strategy**
175	500	70	20	3 mm x 3mm rotating chessboard

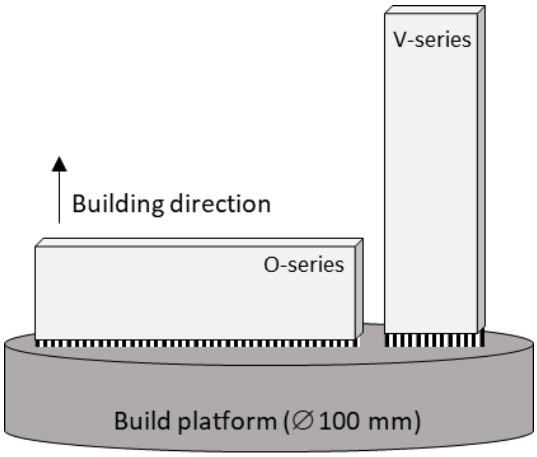

Figure 1: Building orientation of V-series and O-series samples.

After the building process, 18 LPBF samples of the V-series were subjected to two different post aging treatments (9 samples for each). The investigated heat treatment conditions were defined from previous studies (Tonelli et al. 2021) and detailed in Table 3. T6 treatment provides a solution treatment at 540 °C with a holding time of 10 min, followed by a quenching in warm water and a subsequent artificial aging at 150°C for 4 hours. Direct Aging (DA) consist in a shorten artificial aging at 170°C for 1 hour. No O-Series samples were post processed for a comparison with heat treated V-series due to the assumption, well known in the literature, that the typical anisotropy of LPBF samples is reduced or eliminated by post-built heat treatments (Kouraytem et al. 2020).

Table 3: Post-built heat treatment conditions.

	Solution Treatment		**Quenching**	**Artificial Aging**	
	T [°C]	Holding time [min]		T [°C]	Holding time [h]
T6	540	10	Warm water	150	4
DA		Not present	Not present	170	1

Finally, smaller samples (25 mm x 40 mm x 2 mm) were produced with the same LPBF process parameters and post-process (as-built, T6 and DA) conditions for microstructural evaluations and hardness measurements.

2.2. Laser welding

For the welding experiments, the setup consisted of a CW nLight Alta Yb:Fiber laser source with a wavelength of 1070 nm characterized by a maximum output power of 3 kW and a delivery fiber core diameter of 50 µm. The profile of laser beam was Gaussian with a beam product parameter (BPP) <2.8 mm*mrad. The beam was focused and displaced by means of a galvo scanner (Scanlab HurrySCAN 30) equipped by a Wavelength F-Theta fused silica lens with a focal length of 420 mm that allowed a minimum theoretical spot equal to ≈175 µm. The beam directly irradiates the welding zone with the focus on the surface of the samples in the middle of the joint, and no tilting of the welding head was required since the source is equipped with protection devices for against back reflection. The spatial positioning of the galvo scanner on the workpiece was carried out by means of a Yaskawa-Motoman HP-20 anthropomorphic robot. A coaxial camera was also used in order to ensure an accurate positioning of the laser beam with respect to the sheets to be welded. A clamping device, to guarantee the correct position of the samples and achieve ideally zero gap was designed and positioned under the scanning optics. Pure Helium with a flow rate of 10 l min^{-1} was used as shielding gas. Figure 2 shows the laser system setup on the left and a representation of the welded sample on the right.

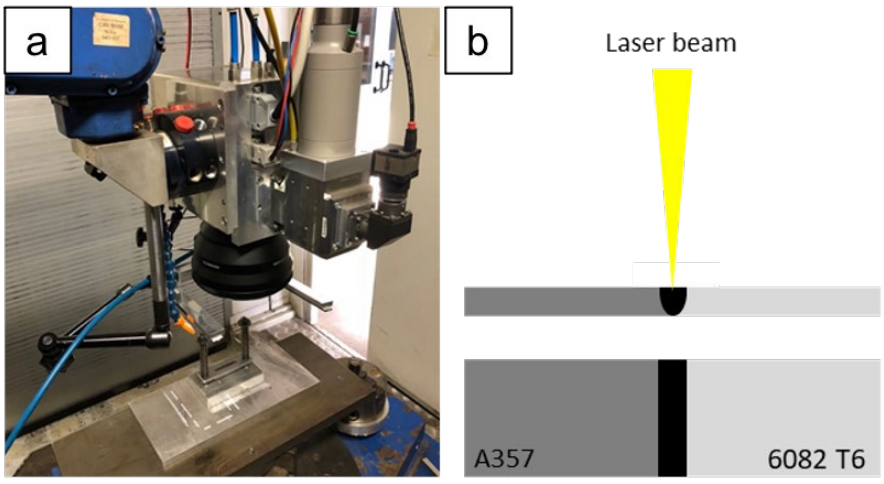

Figure 2: Laser setup for sheets welding (a) and schematic representation of the final welded sample (b).

The LPBF and rolled sheets were welded in butt joint configuration with no filler metal and none special cleaning of the sheets was performed except for the samples produced by LPBF in which the surface roughness was decrease by sandpaper on the edge interested by the welding. A preliminary activity, not discussed in this paper, was carried out in order to define the welding parameters (laser power and welding speed) which allow to obtain a sound joint i.e., a weld seam which includes the whole sheets without excessive dripping in the lower part. From these results, welding parameters have been defined as follows: laser power was kept constant with a value of 1500 W and the welding speed was varied in a range between 40 and 80 mm/s in order to obtain three different linear energy densities (Laser Power/Welding speed). A reference conditions, in terms of weld bead morphology and properties, was established by welding 6082 T6 sheets and LPBF sheets in similar configurations and the results were discussed considering the base materials properties reported in Table 4.

Table 4: Mechanical properties of the base materials: mean values and standard deviation.

Material	Heat treatment	Reference	UTS[MPa]	YS [MPa]	E [%]
AlSi7Mg	As Built	Rao et al.(2017)	426.4±2.6	279.6±1.0	10.1±0.5
	T6-Modified	Pereira et al.(2020)	321±2	271±2	2.9±0.3
	DA	Pereira et al.(2020)	431±16	282±23	6.8±1.4
6082	T6	Matweb (2011)	290	250	10

2.3. Metallographic analysis

Cross-section of the welded samples was prepared by hot mounting the samples in resin and polishing the final surface by using SiC paper with grit from 800 to 2500 followed by 1 µm alumina suspension. The metallurgical specimens for preliminary observation were etched with Keller's reagent (1 ml HF, 1.5 ml HCL, 2.5 ml HNO3 and 95 ml H2O) with an etching time of 20 s. Weld bead morphology of all samples were analyzed by optical microscopy (OM, Nikon Optiphot-100), while average porosity was calculated by means of image analysis by using ImageJ free software. In order to reveal the differences in microstructure due to each process and post-process condition,

electrochemical etching in a Barker solution (ASTM E407) was performed after the previously described samples preparation. Two different voltage and time of exposure were defined for A357 and 6082 sheets, respectively equal to 35 V for 45 s and 50 V for 5 min.

More in-depth microstructural tests were then carried out by SEM-FEG microscope (Tescan Mira3 with Schottky emitter) with EDS system (Bruker X-Flash 630M) for micro elemental analysis.

2.4. Mechanical tests and DIC analysis

After welding, tensile samples with geometry in accordance with standard (BS EN ISO 4136:2011) were obtained by contouring milling operation and the main dimensions are the following: 60 mm in gauge length and 12 mm in width (Figure 3). No other finishing operations were foreseen to reduce the roughness of the LPBF samples.

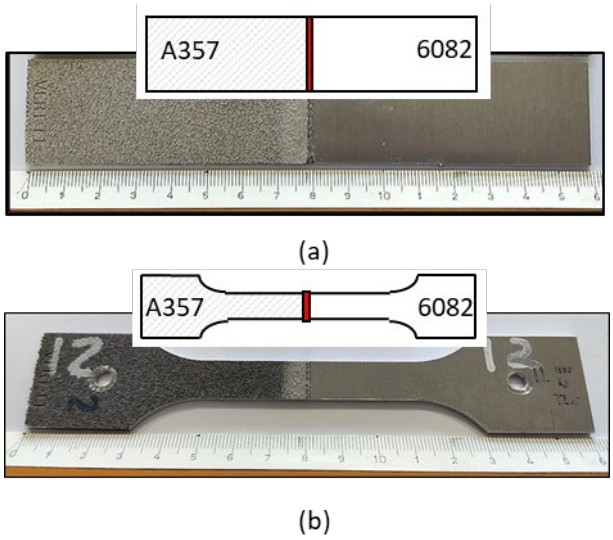

Figure 3: Dissimilar laser welded sheet before (a) and after (b) milling operation.

With respect to LPBF and laser welding parameters mentioned in the previous sections, tensile tests were carried out on 36 hybrid laser-welded tensile samples, of which 9 as-built samples of O-series, 9 as-built samples of V-series, 9 T6 samples of V-series and 9 DA samples of V-series. Together with these tests, 6 additional samples welded under non-hybrid conditions were comprised: 3 samples

6082-6082 and 3 samples A357-A357. All variable process conditions are summarised in Table 5 while laser power was kept constant ad equal to 1500 W.

Room temperature tensile tests were carried out using a hydraulic testing machine (Italsigma S.r.l, Forlì, Italy) with a 20 kN load cell. The strain rate was set to $2.8 \cdot 10^{-4}$ s^{-1} and maintained fixed using a constant cross-head separation rate of 1 mm/min, as required by the tensile testing standard (ISO 6892-1). Two different strain measurement systems were applied on the samples, extensometer (HBM Type DD1, 2.5mV/V) and DIC system, installed on opposite sides of the sheet. Both systems worked throughout the whole loading process until the specimen broke to acquire the strain distribution of the whole field.

Table 5: Summary of the whole experimental plan.

	Welding speed [mm/s]	**Linear energy density [J/mm]**	**Heat treatment**
O-series	40	37,5	None
	60	25	
	80	18,75	
V-series	40	37,5	None
	60	25	
	80	18,75	
	40	37,5	T6
	60	25	
	80	18,75	
	40	37,5	DA
	60	25	
	80	18,75	
REF A357	40	18,75	None
REF 6082	80	37,5	

For DIC analysis, the surface of interest was painted by black little dots on a white background to produce high contrast and random pattern. A 6.4 MPx Basler acA3088-57µm monochrome camera was adopted to capture the frames each 80 N and a customized led-stripes system was positioned behind the camera for the correct illumination of the setup. Figure 4 shows the setup of the tensile tests.

DIC data were processed with GOM Correlate software to obtain the local displacement and strain maps of the interesting area. Fitting data on a longitudinal section was elaborated within MatLab software (version R2019b) in order to obtain specific information of the mechanical behaviour of A357 sheet, 6082 sheet and welded joint.

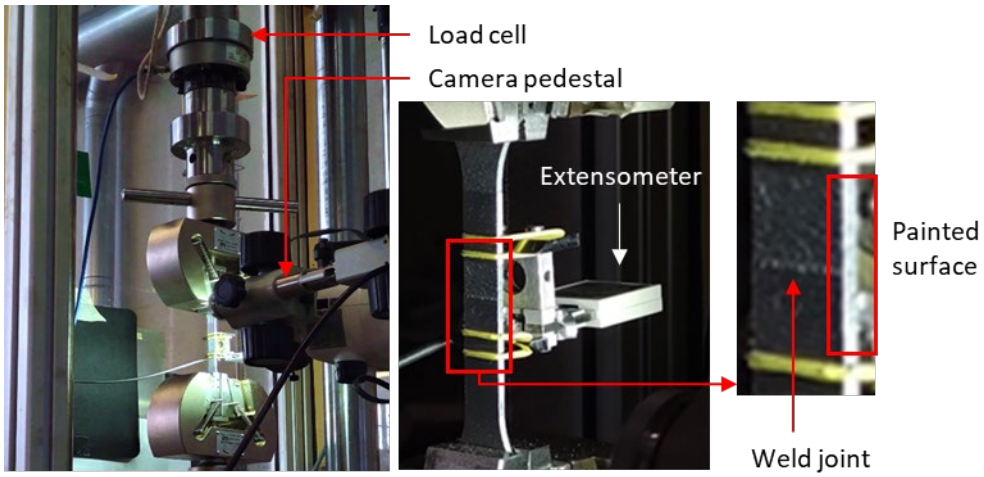

Figure 4: Tensile test setup and measurement systems: in the left, load cell, sample and sample's grip are shown; in the middle the tensile samples is enlarged in order to show the extensometer position and the detail picture on the right highlight the painted surface for DIC analysis.

Longitudinal Vickers microhardness tests were performed using a durometer (HX-1000, Remet) with 0.2 kg load (HV0.2) and dwell time of 10 s on metallographic samples described in the previous section (Figure 5). Over 25 indentations were carried out to analyse the hardness profile of each samples, with a space between each indentation of 250 µm on the base material and 150 µm inside the joint.

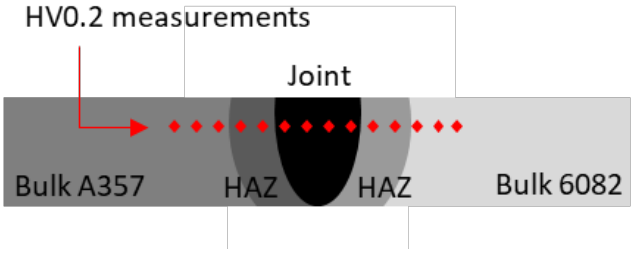

Figure 5: Vickers micro-hardness test position.

3. Results

3.1. Metallographic analysis

The cross sections of the hybrid weld seam obtained with different welding parameters are shown in Figure 6; on the left side of the welded samples are the LPBF sheets while on the right side the sheets of 6082. It can be noted that complete welding of the two sheets was obtained for all the combinations. Despite the lower magnification, no solidification cracks were found in the joints even though the welding was carried out without filler metal. Once cross-sections were obtained, it was possible to measure the geometric characteristics of the weld seam, in particular the weld width on the top surface.

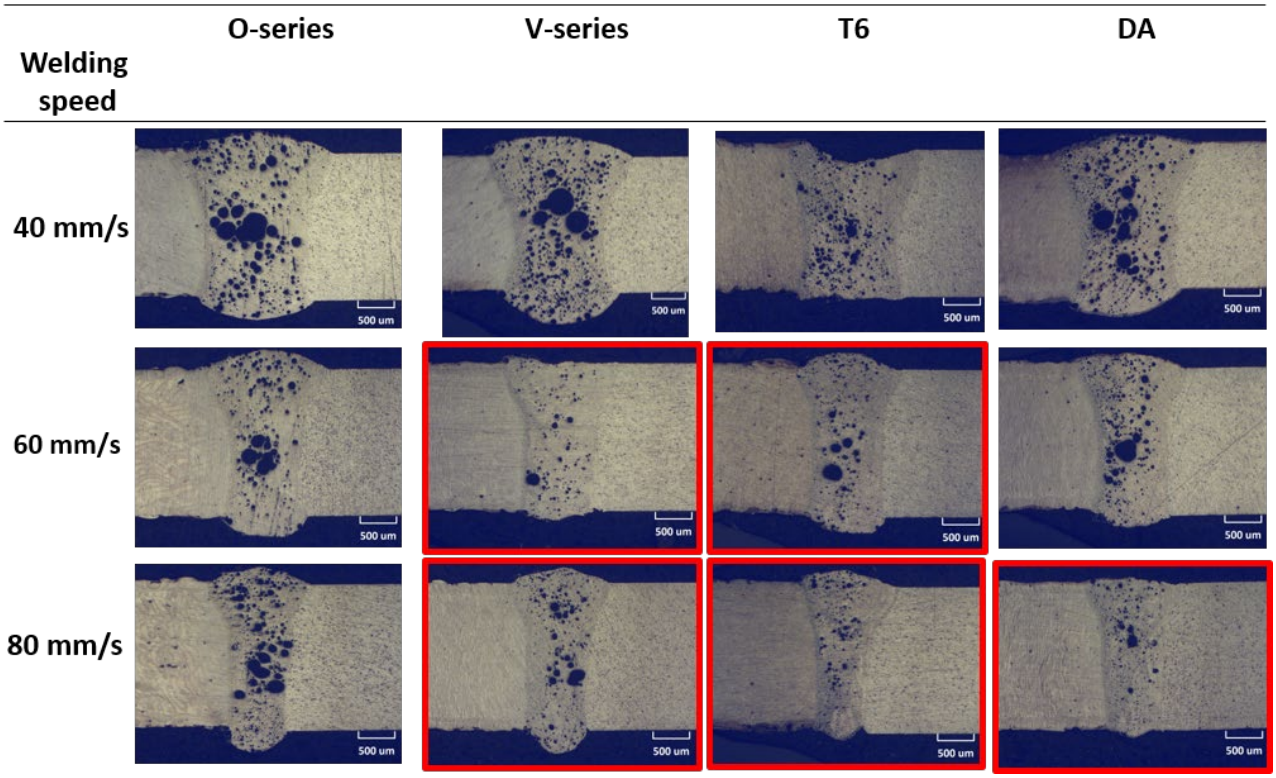

Figure 6: Optical microscope cross-sections of the welded samples.

The width decreases as the welding speed increases since the heat input, in terms of linear energy density, decreases as well. Values of about 2.6 mm were measured with welding speed of 40 mm/s, while at the highest welding speed of 80 mm/s the weld width is about 2.2 mm. It can be concluded

that the morphology of the weld bead is much more influenced by the welding parameters, even though the difference is small, than by the LPBF orientation and post-processing conditions of the A357 sheets.

Porosity formation is considered one of the most common and serious defects which occurs during laser beam welding of aluminum alloys, as reported by Xu J. et al. in (2018). Presence of pores inside the weld seam is deleterious since negatively affects the mechanical properties of the joint. Porosity measurement results, in terms of percentage of fused area, are shown in Figure 7.

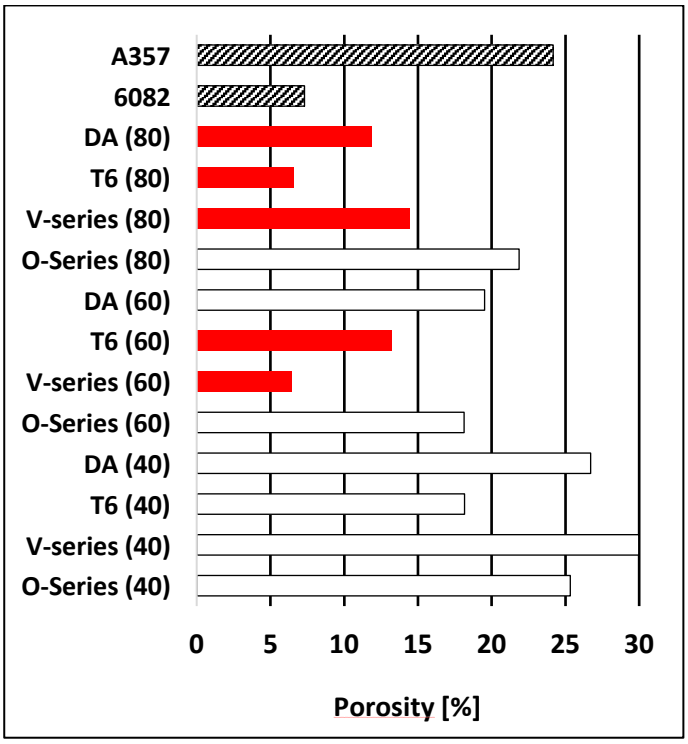

Figure 7: Porosity of reference (striped bars) and hybrid (full coloured) weld beads measured by imaging evaluation. Red bars indicate the welding conditions with less porosity.

From data analysis, in A357-A357 welded sheets the percentage of porosity is about 24 %, while for the 6082-6082 is about 7 %. For the hybrid weld seams, the higher presence of porosity was measured at welding speed of 40 mm/s, where pores of higher dimensions (mainly 100-200 µm) were also detected, confirming what observed in the cross-section images of Figure 6. On the other

hand, by increasing the welding speed, except for the O-series samples, the percentage of porosity decreases; the lower value of 6.4% was obtained for the welding speed of 80 mm/s on A357-T6 samples. Along with this percentage reduction, a decreasing of pores average size has been identified. Red frames highlight the welding conditions with less porosity in Figure 6 and red bars of Figure 7 confirm this result. Lastly, it worth noting that the pores are distributed in most cases along the center of the joint and close to the LPBF sheet.

Optical micrographs after the electrochemical etching were performed in order to highlight the microstructural differences as the process and post-process conditions of the A357 sheets vary and in the three different regions of interest: LPBF printed A357, rolled 6068 and welded joint. Figure 8 shows low magnification OM images of these 3 parts of the samples: in the left side the microstructural variations of A357 as-built samples (O-series and V-series) and post heat treated ones (T6 and DA) is highlighted, in the right side is shown the 6082 bulk microstructure and in the centre the weld joint and the Heat Affected Zone (HAZ) microstructure. As-built A357 conditions for both orientations are characterised by well-defined and overlapped melt pool boundaries. The pool boundaries are shown in darker contrast respect to the centre of the melt pool (Figure 8a).

OM images reveal the geometry of grains, elongated in the build direction, as vertically built samples show, and with an equiaxed section, evident in O-series picture. This grain morphology, well known in literature (Bahl et al., 2021 and Charmi et al. 2021) is one of the main reasons of LPBF as-built components anisotropy, which properties are therefore building-direction dependent. After a DA heat treatment, microstructure variations are not properly noticeable by optical images and the melt pool boundaries continues to be well marked. Conversely, complete solubilisation and artificial aging treatment (T6) have substantially modified the microstructure. From OM picture the molten pool boundaries remain clearly visible, but not disappeared as Yang et al. (2018) and Pereira et al. (2020) claim, and inside the pools several Si particles are visible, in particular along the big grains

edge, as stated by Mauduit et al. (2019). The microstructure of the 6082 base material is illustrated in the right side (Figure 8e): it consists mainly of 40-50 µm grains slightly elongated in the rolling direction, though several equiaxed grains coexist in the structure. No in-depth analysis was carried out on commercial 6082 sheet. As concern the weld bead microstructure it possible to identify a well-defined HAZ with a thickness of about 100 µm with coarse dendrites (Figure 8b,d) and a fully fused zone (FZ) with primary α-Al dendrites and a α-Al/Si eutectic (Figure 8c).

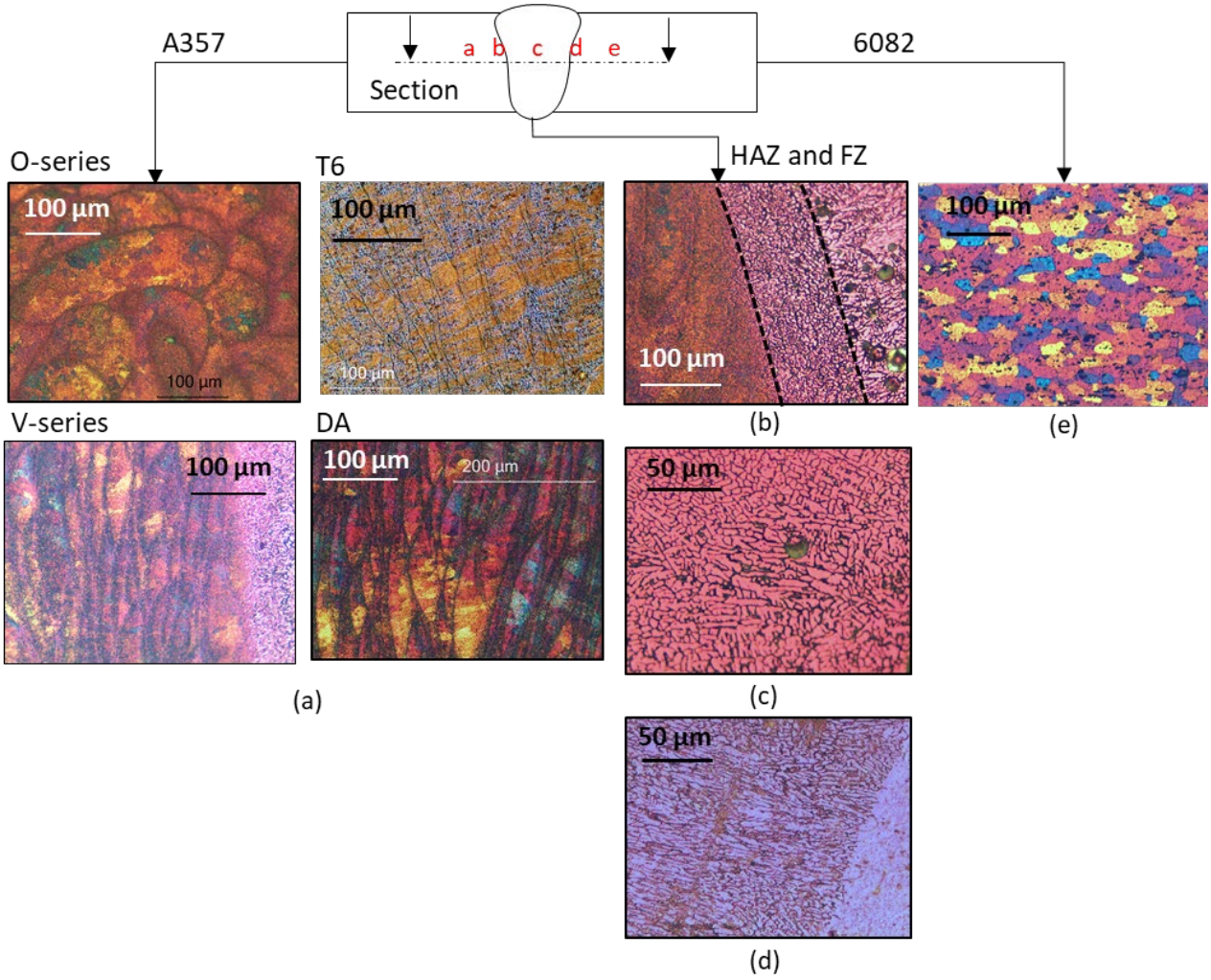

Figure 8: Microstructure of A357 (a), weld bead (b,c,d) and 6082 (e) parts revealed by OM. A357 microstructure is shown for as built samples (O-series and V-series) and heat-treated samples (T6 and DA). The weld bead images highlight both the HAZs (b,d) and the FZ (c).

SEM analysis of microstructural evolution in HAZ and FZ is reported in Figure 9 for as built samples: starting from the HAZ of A357 part (Figure 9 a,b) the microstructure consists in columnar grains growing from the fusion line to the centre of the weld bead. The centre of the weld is composed of equiaxed grains, as shown in Figure 9c. Moving towards the 6082 side, once again columnar grains, with bigger dimension, were detected (Figure 9d) to the end of the HAZ (Figure 9e). The chemical composition analysis at the centre of the weld bead (zone c in Figure 9) by means of EDS were carried out with the aim to obtain information about the main elements which characterize the fused zone. High magnification SEM images is shown in the left side of Figure 10. As stated before, the FZ mainly consists of primary α-Al dendrites (Spectrum 2) while the grain boundaries (Spectrum 1) are rich in Si (12 wt%) and Mg (0.6 wt%).

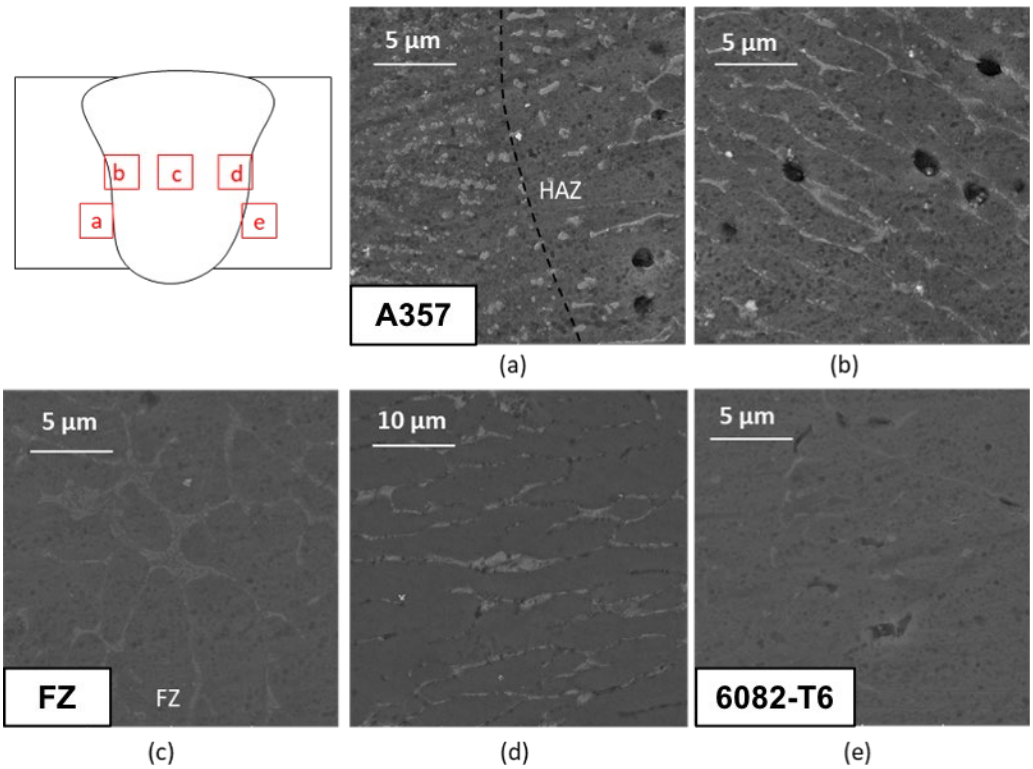

Figure 9: SEM analysis of the weld bead: the microstructural evolution from A357-HAZ (a) to 6082-HAZ (e).

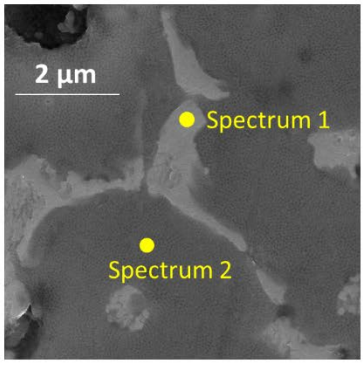

[wt%]	Al	Si	Mg
Spectrum 1	87.11	12.29	0.6
Spectrum 2	96.48	3.32	0.2

(a)

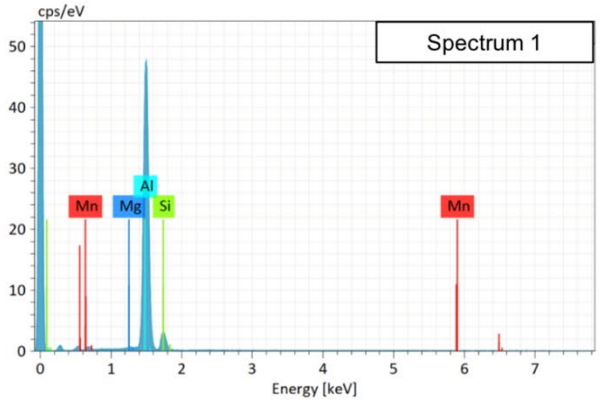

(b)

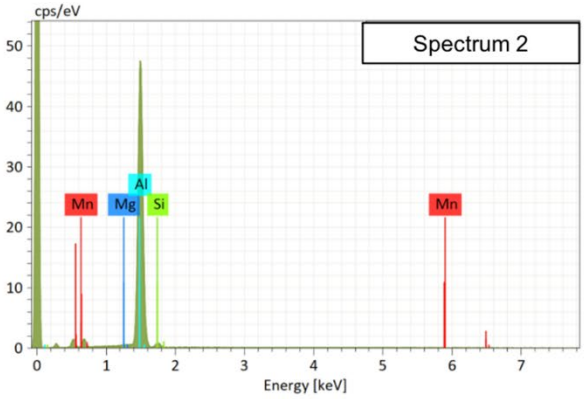

(c)

Figure 10: EDS analysis in the centre of FZ of hybrid samples obtained welding V_Series-A357 part with 6082(a) at 40 mm/s, spectrum of probe point 1 (b) and spectrum of probe point (c).

EDS analysis was carried out also in the FZ of hybrid samples obtained by welding at 40 mm/s the T6-A357 part with T6-6082. In this process condition, a large amount of needle-like intergranular precipitates were identified, as shown in Figure 11. Spectrum 3 revealed a high quantity of Fe, Mn, Mg and Si respect to the surrounding base material (Spectrum 4)

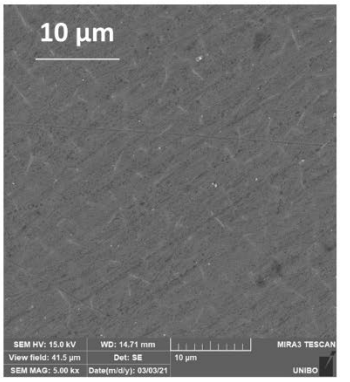

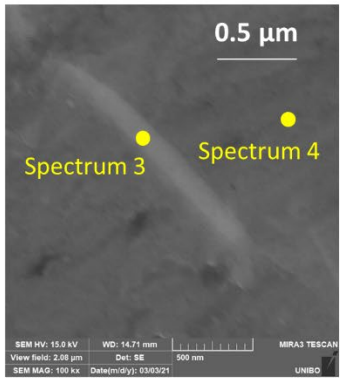

[wt%]	Al	Si	Mg	Mn	Fe
Spectrum 3	81.28	11.05	0.64	2.95	4.08
Spectrum 4	97.30	1.93	0.28	0.34	0.14

(a)

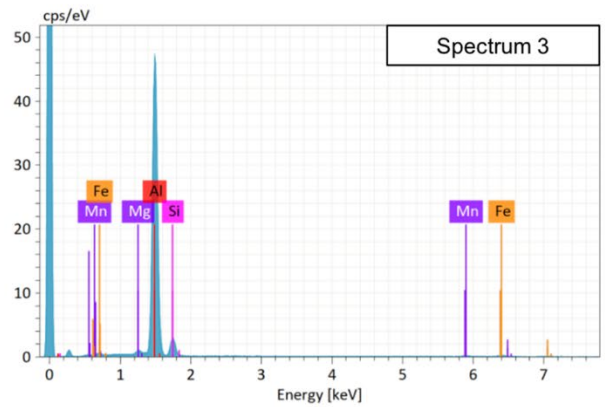

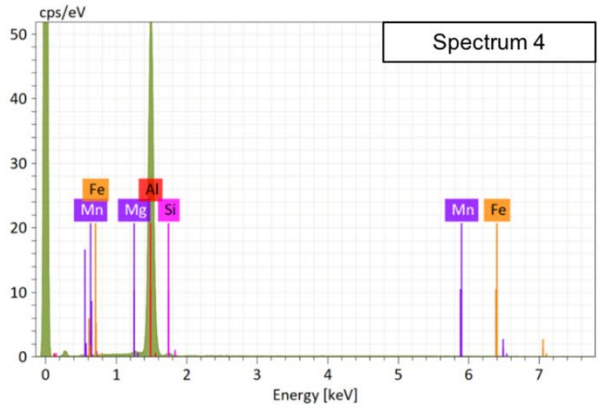

(b) (c)

Figure 11: EDS analysis in the centre of FZ (left) and in 6082-HAZ (right) of hybrid samples obtained welding T6-A357 part with 6082(a) at 40 mm/s, spectrum of probe point 3 (b) and spectrum of probe point 4(c).

3.2. Tensile properties

Tensile properties together with the standard deviation results are displayed in Table 6 and a focus on engineering stress-strain behaviour in Figure 12. The mechanical characteristics are consistent between repetitions and the main effects of post heat treatment on A357 sheets are confirmed when the welding parameters change.

Table 6: Tensile tests results.

	Welding speed [mm/s]	Mean UTS [MPa]	Std. Dev.	Mean YS [MPa]	Std. Dev.	Mean Elongation [%]	Std. Dev.
O-series	40	121	0.8	/		0.29	0.03
	60	129	4.1			0.26	0.04
	80	138	11.1			0.30	0.01
V-series	40	119	6.4			0.36	0.01
	60	158	8.5			0.31	0.07
	80	156	7.5			0.36	0.08
T6	40	232	5.1	202	7.6	0.81	0.21
	60	173	2.5	123	24.7	5.72	6.54
	80	186	17.1	148	24.7	1.35	1.39
DA	40	148	6.1	/		0.41	0.02
	60	162	5.7			0.32	0.08
	80	178	0.9			0.36	0.00
REF A357	80	114	3.3	/		0.32	0.01
REF 6082	40	248	2.7	178	6.4	2.31	0.17

From data analysis, 6082-6082 welding sheet presents the higher Ultimate Tensile Strength (UTS) and elongation, respectively equal to 248 MPa and 2.31 %, while A357-A357 samples, in contrast to the previous reference condition, show the lowest UTS value (114 MPa) and an elongation of 0.32 %. Hybrid joints with as-built LPBF parts show similar elongation of the reference A357-A357 condition, but higher strength, in particular at welding speed increasing, reaching values up to 158 MPa. DA treatments reinforce the A357 sheet with a positive influence also in the joint strength. UTS value increases, in comparison with V-series, up to 20 % and as previously noted, the increase in UTS is strongly related to the increase in welding speed. Finally, the complete T6 heat treatment is the reason of a ductile behaviour improvement of the samples that clearly show the transition between elastic and plastic behaviour, unlike the previous cases, allowing to calculate the yield strength (YS) value as the stress at which a 0.2 % of deformation occurs. Unexpected higher UTS values were measured in case of 40 mm/s welded joint (232 MPa) in comparison to samples obtained with higher speed (173 MPa and 186 MPa), despite the measured porosity of the joint was grater in the first case. However, this result is in line with the microstructure analysis which showed

the presence of intermetallic in these process condition that usually contribute to the dispersion strengthening of Al-alloys (Yang et al., 2018).

The described results, discussed more in detail in the next section, can be interpreted by considering that the welding speed, and consequently the amount of porosity, mainly determines the strength increasing of the samples. In case of higher welding speed, DA post heat treatment acquire also a more significant effect on mechanical properties, as clear by comparing Figure 12a and 12b, while building orientation (O-series vs V-series) maintain a negligible effect in all tested conditions.

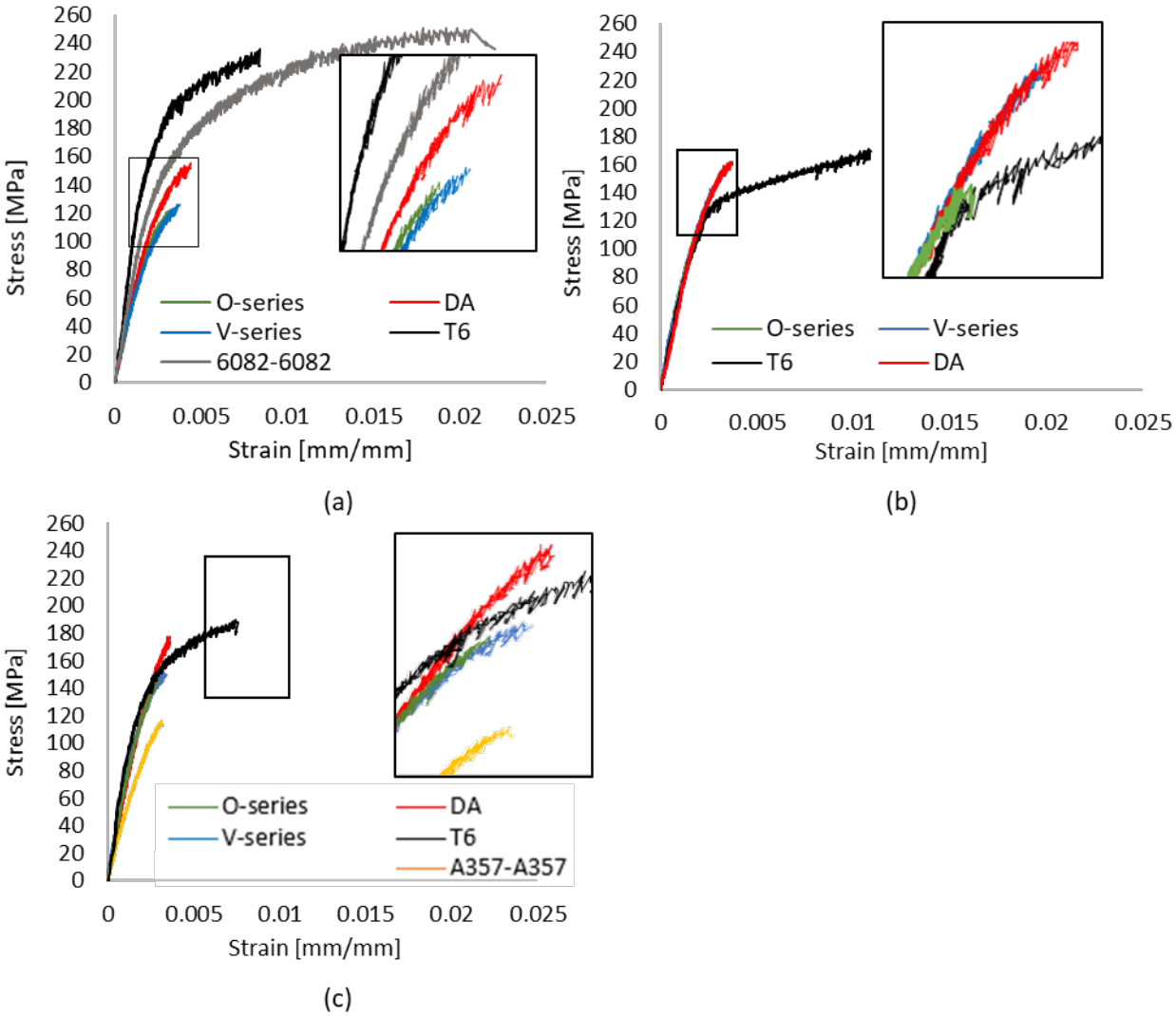

Figure 12: Stress-strain curves obtained for samples welded at 40 mm/s (a), 60 mm/s (b) and 80 mm/s (c).

3.3. Hardness measurements

Vickers microhardness longitudinal variations are displayed in Figure 13. Samples welded at 40 mm/s were selected for results discussion due the higher extension of weld joint that allows to show clearer graph of the obtained results.

FZ and HAZ are highlight with different colours, respectively red and blue, while the bulk material is located on the sides of these regions and a mean hardness value is reported with a red arrow. While the mean hardness of 6082 bulk sheet (130 $HV_{0.2}$) does not change as expected, the mean hardness in the A357 side vary with the building orientation ad post treatment from a minimum value (113 $HV_{0.2}$) in case of T6 heat treatment and a maximum (136 $HV_{0.2}$) for DA treated samples. As-built sheets have intermediate hardness, lower in case of O-series (118 $HV_{0.2}$) in comparison to V-series (130 $HV_{0.2}$).

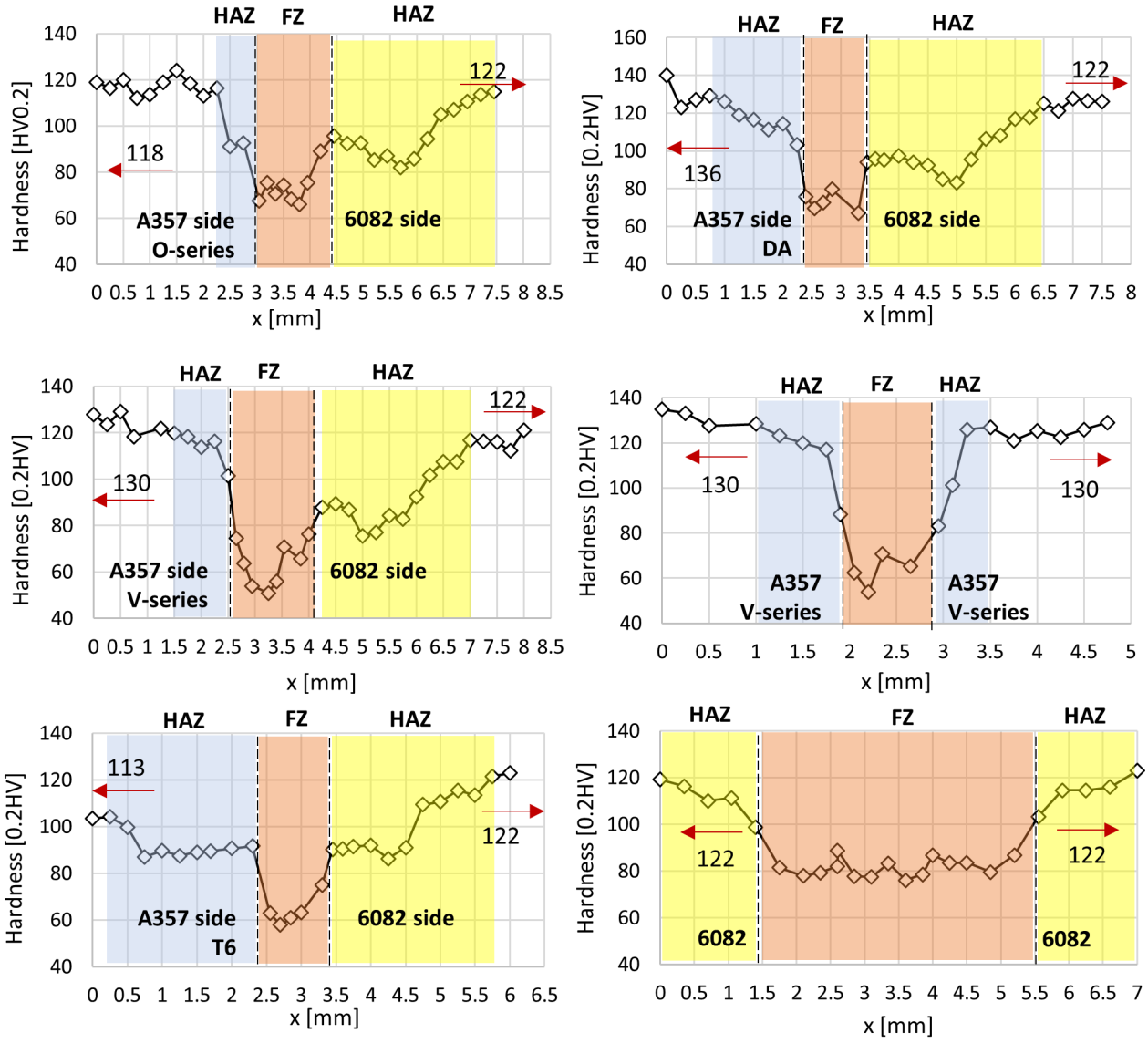

Figure 13: Hardness profile of the weld joint cross-section. Red areas represent the FZ, blue and yellow areas show the HAZ respectively on LPBF (A357) and rolled sheet (6082) side.

It worth to note the hardness variation close to the joint edges: from the A357 side (left side in Figure 13) the hardness in the HAZ area continuously increase with a quite steep slope except for T6 condition, in which the bulk value is reached in two successive steps. Conversely, from 6082 side (right side in Figure 13) it is possible to identify a first growth in hardness followed by a relative minimum and then a new growth until the bulk material value is reached.

3.4. DIC results

The DIC-estimated εy local strain behaviour is reported in Figures 14 and 15; the behaviour of 40 mm/s welded samples were used for present the obtained results for continuity with the previous section. Engineering strains were evaluated at the last frame before fracture in a longitudinal section of the sample, as shown in the top part of each pictures.

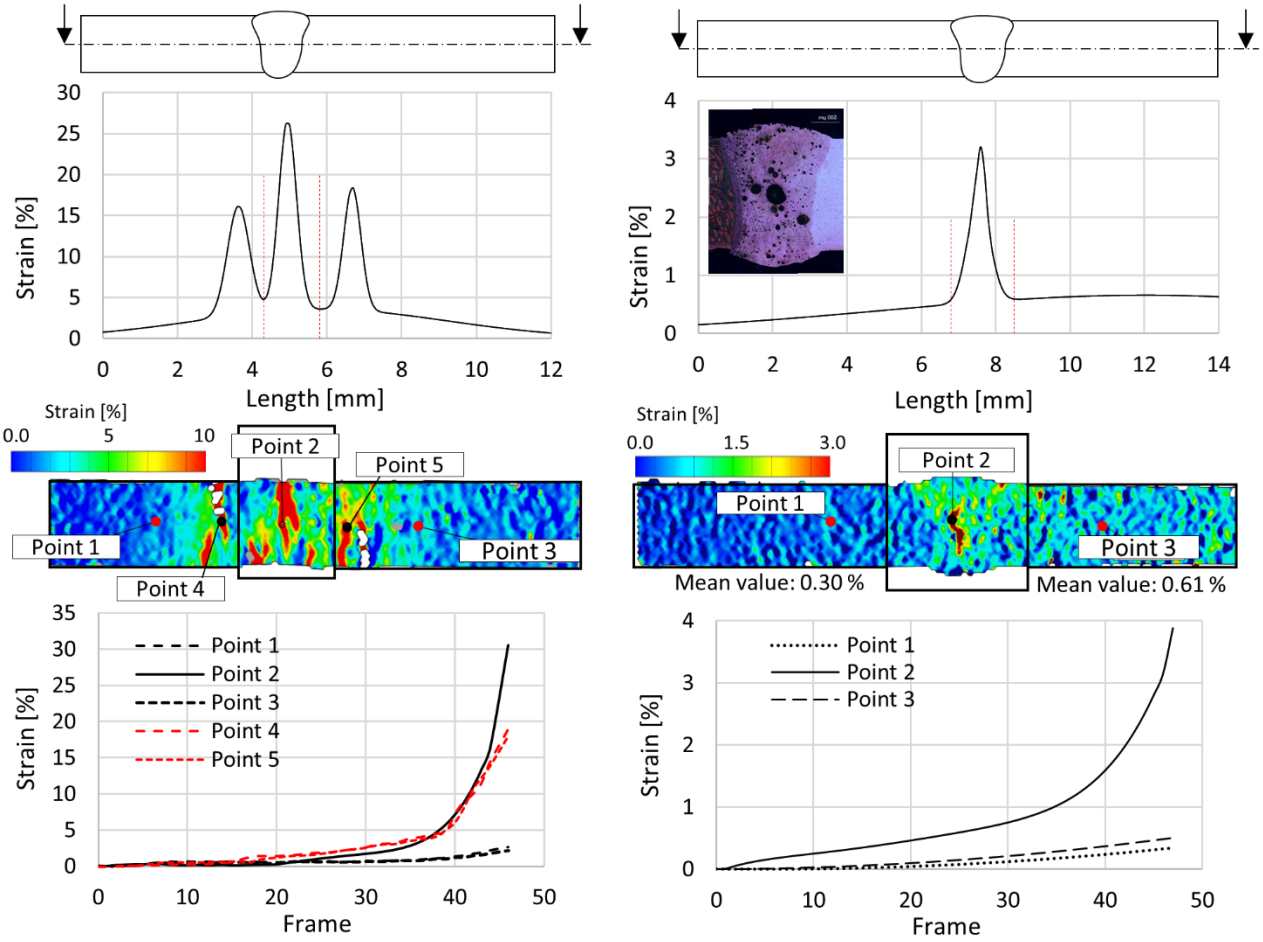

Figure 14: Strain distribution on a longitudinal section, strain maps and strain evolution in three reference points of 6082-6082 (a) and O-series (b).

Together with the line diagram, 2D strain coloured map of the observed surface at the same frame is reported, highlighting local peaks corresponding to the failure areas. In order to underline the differences in the 3 main regions of interest of the welded sheets, the strain during the entire tensile test (from frame 0 to sample failure) of 3 probe points is shown in the bottom of the Figures. Point

2 is located in the centre of the joint, while Point 1 and Point 3 are aligned with Point 1 along y and spaced 3 mm from it. In particular, Point 1 is referred to A357 sheet (excluding the 6082-6082 reference condition of Figure 14) and Point 3 to 6082 sheet.

From diagrams and maps comparison analysis several considerations can be done. All samples present a peak of strain in the middle of the weld joint and the maximum peak value is strictly correlate to the ductility of the sample and consequently to the post process condition of A357 part. In particular, as expected higher peak values of local strain correspond to higher elongations measured with tensile tests (Table 5) and the ratio between local and global engineering deformation is in the range of 7.5-10.5.

Post heat treated hybrid samples (Figure 15), clearly show a second peak of strain in the HAZ area close to 6082 sheets unlike what was detected in the as-built samples (Figure 14(b)). From a more accurate assessment of strains' map, as-built samples exhibit an accumulation of deformation in the same HAZ area, however it is less pronounced and concentrated near the top surface of the samples, so it is not highlighted in the middle longitudinal section. Under T6 condition, strain trend exhibit a third peak in the A357 HAZ side, as well as in the reference case of 6082-6082 welded sheet, albeit with less pronounced values. Indeed, 6082-6082 sample show laterals strain peaks in both the HAZ regions and these values overcome the 15% of engineering strain. The deformation growth in HAZ follows that of FZ, that reveals a higher peak only in the last frames.

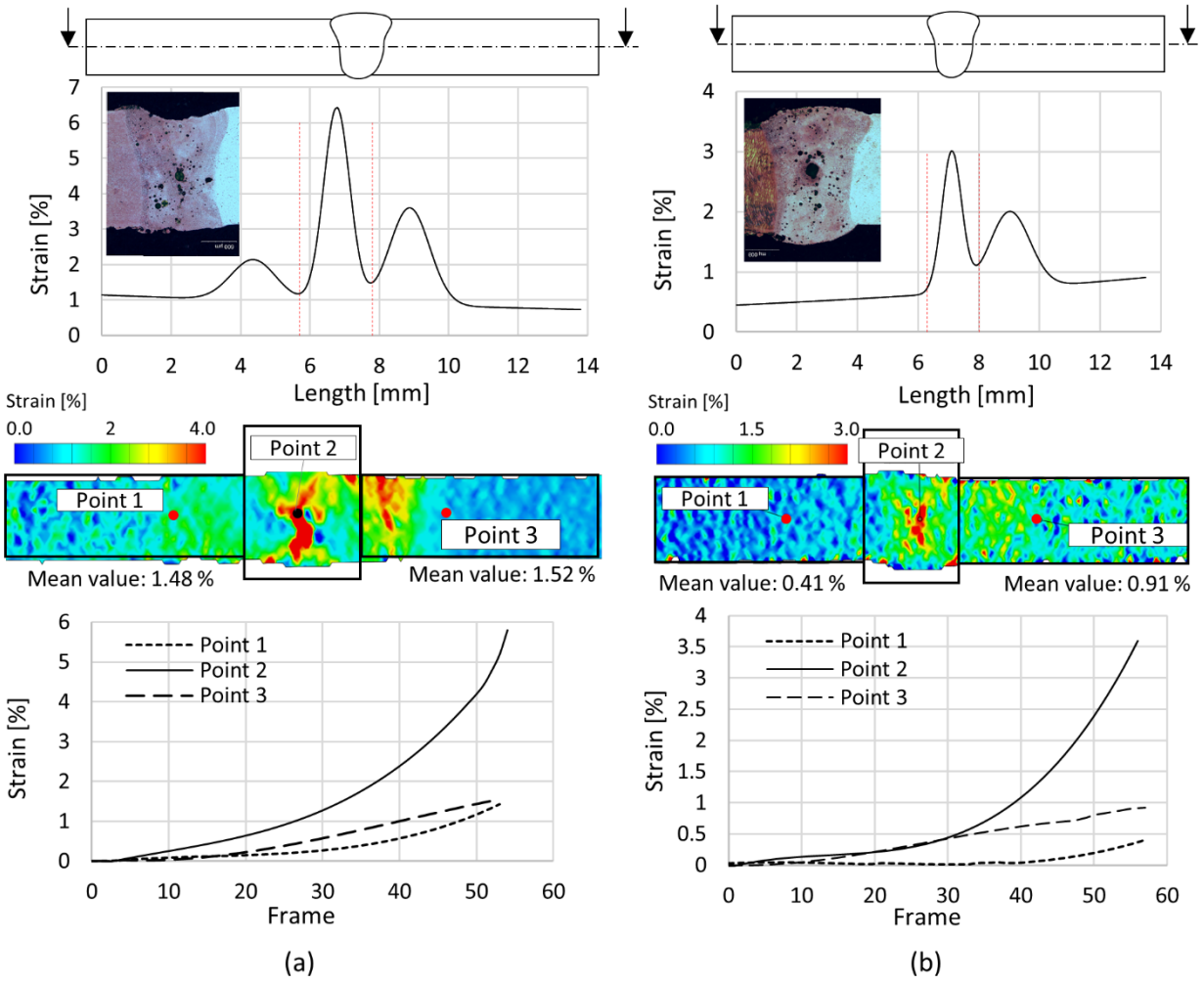

Figure 15: Strain distribution on a longitudinal section, strain maps and strain evolution in three reference points of T6 (a) and DA (b) samples.

The deformation degree in the bulk material region is substantially negligible relative to the FZ and HAZ zones in all cases, as shown by the probe points strain evolution during the tests. The deformation increasing during the tests is approximately linear far from the FZ, while in the centre of the weald bead it is possible to distinguish a first stage with a slow strain growth followed by a steep increasing up to the sample failure. Figure 16 summarise FZ, HAZs and Bulk regions mean strain values extrapolated by DIC measurements, as arithmetic mean of the values assumed by each pixel, together with data standard deviation, for all 40 mm/s welded samples.

Deformation behaviour at higher laser speed maintain same characteristics but on smaller areas, in particular for HAZ region, so more difficult to be expressed as a reliable average value.

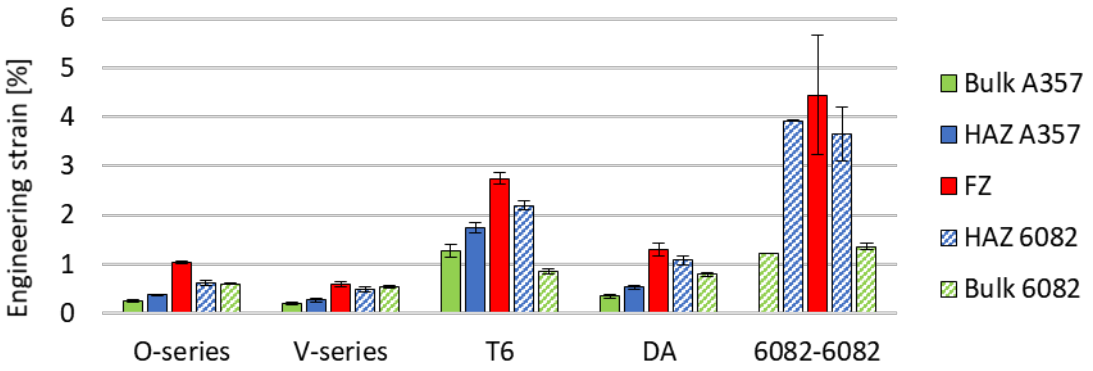

Figure 16: Engineering strain mean values measured by DIC in FZ, HAZ and bulk areas

4. Discussion

The main proposed applications for AM processes nowadays are related to the design of high-complexity products; however, components' dimension often precludes the use of these processes in different industrial sector as automotive. A possible solution is to investigate joint's processes between AM parts, characterized by high-customizable design, and conventional products. In this view, the presented work has determined the feasibility of laser technology to join thin sheets in dissimilar configuration: commercial 6082-T6 sheet produced by conventional hot rolling with A357 part produced by LPBF. The effects of LPBF building orientation and post-process conditions and the laser welding parameters were studied by mechanical and microstructural point of view.

4.1 Weld bead morphology and microstructure

In Figure 6 the morphology of the weld seam obtained by means of optical microscope was reported. It is evident that the weld bead width increases as the welding speed decreases due to the rises of the heat input, in terms of linear energy density; this is in accordance with what found and discussed by Sanchez-Amaya et al. (2009). Still analysing the images reported in Figure 6, it was

possible to identify the geometry of the porosities: regular round shape defects were detected and therefore can be traced back to metallurgical porosities, as confirmed by Li et al. (2015). One of the key points, in deep penetration welding of aluminum alloys, on which the success of the process depends, is represented by the stability of the keyhole determined in turn by different forces such as, recoil pressure, surface tension, hydrodynamic and hydrostatic pressure. As the heat input increases the recoil pressure increases as well which lead to the unbalance of the forces resulting in the instability and collapse of the keyhole; therefore, the gas inside gets isolated and bubbles are formed. As concern the welding parameters, there is a clear beneficial effect of increasing the welding speed, since the weld bead width dimension is reduced slightly from 40 mm/s to 80 mm/s, while the presence of pores and their size are drastically reduced in all the testes conditions. These results agree with previously studied and analysed by other authors; for example, Norris et al. (2011) found that more pores can be generated at lower welding speed and the average size of porosity increases when heat input increases as well; Fetzer et al. (2021) also confirms that the stability of the keyhole and therefore the presence of pores, during laser beam welding of AlMgSi alloys, increases as the welding speed increases.

SEM/FEG analysis has highlighted the microstructure evolution of weld bead, which includes, in the central area of the joints, equiaxed grains and columnar grains growing from the base metal to the centre. In the centre of the weld bead, the highest temperature gradient direction corresponds to the welding direction and consequently in the joint centreline the dendrites grow into axial grains along the heat flux, as highlighted by Wang et al. (2016). The change in grains growth takes place where the difference in temperature occurred. As concern the specific microstructure of FZ, EDS measurement highlights dendritic α-Al matrix with eutectic Si at the edges, in accordance to what found in a previous study conducted by Nahmany et al. (2017). Intergranular precipitates which

contain Fe, Si, Mg and Mn has been found only in T6-A357 parts welded with 6082 sheets at 40 mm/s.

4.2 Mechanical properties

Tensile tests have proved that 6082-6082 welding sheet presents the higher UTS and elongation due to the combined effect of the bulk material properties (Table 4) and the lower porosity percentage in the joint. In contrast to the previous reference condition, A357-A357 samples show the lowest UTS and strain values. These results are strongly influenced by the quality of the weld bead because in as-built conditions A357 reaches UTS values of 400 MPa and elongation up to 8%, as demonstrated by Rao et al. (2017). Considering the building orientation, O-series shows a mean elongation slightly higher than V-series for all welding speed condition, as expected from data reported by Oliveira de Menezes et al. (2019). However, the high porosity hides substantial differences and make this process variable negligible. Conversely, LPBF post-process affect the mechanical properties of the joined sheets, in particular DA reinforcement of the A357 sheet leads to an UTS value increasing up to 20 % and T6 up to 90 % corresponding to strength values close to those obtained for 6082-6082 condition. This last evaluation, however, is not only related to the microstructural change, but on the quality of the joint that can be obtained, as highlighted by hardness measurements. In fact, connecting back as shown in the Figure 13 with the last consideration about the tensile properties, A357 T6 samples present a mean bulk hardness (113 $HV_{0.2}$) lower than the other process conditions that return values up to 130 $HV_{0.2}$. While this result validates the increase in ductility of these samples, it is not compatible with the increase in strength, which can consequently be explained only through a better result in terms of weldability of the T6 component respect to the as-built state. An interesting result concern the T6 components strength is related to the welding speed: UTS of these joints is maximum for lower welding speeds (25 % higher at 40 mm/s than at 80 mm/s, in contrast with the UTS behaviour obtained in the other

process conditions. As mentioned in the results section, SEM analysis revealed the presence of Fe-rich intermetallic phases only in T6 joints welded at 40 mm/s. The formation of this compound is probably linked to the slower solidification rates that interest these samples respect to the other (Murali et al., 1992) and can be responsible to the highlighted strengthening.

Softening in both FZ and HAZ is the result of recrystallization due to heat input supplied during the welding, as demonstrated in Figure 9 but also due to the loss of strengthening phases and segregation of Si to the grain boundaries, as shown in Figure 10, thus eliminating solid solution hardening as highlighted by Pakdil et al. (2011).

DIC analysis revealed that the main strain peaks identified in the center of FZ correspond to lower hardness and to the failure zone of all samples. Secondary peaks instead are associated with the extension of HAZ: all samples have shown a well-defined HAZ, with lower hardness, from the side of 6082 responsible for the second peak of deformations. The lack of a relative maximum of the deformations in the A357-HAZ part of as-built and DA conditions agrees with hardness measurements: form this side the extension of HAZ is limited and the increase in hardness is sudden. A possible explanation of the obtained data is the lower thermal conductivity of A357 compared to 6082 alloy. This statement seems to be confirmed by the results of hybrid sheet welded after T6 treatment of A357. In this configuration a third strain peak becomes evident also in the LPBF part and the hardness diagram show a greater extension of the HAZ similarly to 6082-6082 behavior. Indeed, after T6 heat treatment the thermal conductivity of the alloy increases, as demonstrated by Butler et al. (2021) that have measured an increase of conductivity between 20 and 30% on AlSi10Mg alloy, produced with LPBF, after heat treatment. Obviously, in addition to this, the T6 treatment makes the A357 more ductile as confirmed by the hardness value of the bulk and by the tensile tests elongations results.

5. Conclusion

Microstructural and mechanical characterization of 2 mm thick sheet laser welded in butt-joint dissimilar configuration have been presented in this paper. Experiments have been carried out with the aim of investigating the behavior of joint at different process and post-process parameters, in particular laser welding speed, LPBF sheet orientation and post build heat treatment.

The experimental results show that at welding speed of 80 mm/s it is possible to produce a weld bead with porosities comparable to the reference condition represented by 6082-6082 welding. The results also highlight the fact that post build heat treatment of LPBF sheet has the strongest influence on final properties of the joint, while building orientation do not induce significant effects over the tested range. Tensile tests revealed that a complete T6 heat treatment on LPBF sheets leads to UTS and elongation values close to those obtained for 6082-6082 due to an increase in weldability and ductility of LPBF sheets. DIC tests confirmed these results and revealed that after T6, the sheet deformation during tensile test, in addition to the main peak localized in the FZ, show secondary peaks in both HAZs. This behavior corresponds to a more extended HAZ of T6-A357 sheet respect to as-built and DA conditions, as established also by micro-hardness analysis carried out longitudinally to the joint, which show similar trend of T6-A357 and 6082 alloys.

Data availability

The dataset analyzed during the current study are available from the corresponding author on reasonable request.

Declaration of Competing Interest

The authors declare no competing interest.

CRediT authorship contribution statement

Vincenzo Dimatteo: Experimental Investigation, Data curation, Writing – original draft. **Erica Liverani:** Conceptualization, Methodology, Software, Writing – review & editing. **Alessandro Ascari:** Investigation, Data analysis, Supervision. **Alessandro Fortunato:** Supervision, Validation, Writing – review & editing.

Reference

Ascari, A., Fortunato, A., Liverani, E., Gamberoni, E., Tomesani, L., 2016. New possibilities in the fabrication of hybrid components with big dimensions by means of selective laser melting (SLM). 9th International Conference on Photonic technologies – LANE 2016. Physics Procedia. 83, 839-846. https://doi.org/10.1016/j.phpro.2016.08.087

Bahl, S. Mishra, S., Yazar, K. U., Kola, I. R., Chatterjee, K., Suwas, S., 2019. Non-equilibrium microstructure, crystallographic texture and morphological texture synergistically result in unusual mechanical properties of 3D printed 316L stainless steel. Additive Manufacturing. 28, 65-77. https://doi.org/10.1016/j.addma.2019.04.016

Butler, C., Babu, S., Lundy, R., O'Reilly Meehan, R., Punch, J., Jeffers, N., 2021. Effects of processing parameters and heat treatment on thermal conductivity of additively manufactured AlSi10Mg by selective laser melting. Materials Characterization. 173, 110945. https://doi.org/10.1016/j.matchar.2021.110945

Charmi, A., Falkenberg, R., Ávila, L., Mohr, G., Sommer, K., Ulbricht, A., Sprengel, M., Saliwan Neumann, R., Skrotzki, B., Evans, A., 2021. Mechanical anisotropy of additively manufactured stainless steel 316L: An experimental and numerical study. Materials Science and Engineering A. 799, 140154. https://doi.org/10.1016/j.msea.2020.140154

Commision E, 2017. Reducing CO_2 emissions from passenger cars.

Du, Z., Chen, H.C., Tan, M.J., Bi, J., Chua, C.K., 2018. Investigation of porosity reduction, microstructure and mechanical properties for joining of selective laser melting fabricated aluminium

composite via friction stir welding. Journal of Manufacturing Processes. 36,33-43. https://doi.org/10.1016/j.jmapro.2018.09.024

Fetzer, F., Hagenlocher, C., Weber, R., Graf, T., 2021. Geometry and stability of the capillary during deep-penetration laser welding of AlMgSi at high feed rates. Optics and Laser Technology. 133, 106562. https://doi.org/10.1016/j.optlastec.2020.106562

Holker, R., Haase, M., Khalifa, N.B., Tekkaya, E., 2015. Hot extrusion dies with conformal cooling channels produced by additive manufacturing. Materials Today: Proceedings. 2, 4838-4846. https://doi.org/10.1016/j.matpr.2015.10.028

Hong, K and Shin, Y., 2017. Prospects of laser welding technology in the automotive industry: A review. Journal of Materials Processing Technology. 245,46-49. https://doi.org/10.1016/j.jmatprotec.2017.02.008

Kouraytem, N., Varga, J., Amin-Ahmadi, B., Mirmohammad, H., Chanut, R.A., Spear, A.D., Kingstedt, O.T., 2020. A recrystallization heat-treatment to reduce deformation anisotropy of additively manufactured Inconel 718. Materials & Design. 198,109228. https://doi.org/10.1016/j.matdes.2020.109228

Li, K., Lu, F., Guo, S., Cui, H., Tang, X., 2015. Porosity sensitivity of A356 Al alloy during fiber laser welding. Transactions of Nonferrous Metals Society of China. 25, 2516-2523. https://doi.org/10.1016/S1003-6326(15)63870-5

Matweb, 2001. www.matweb.com

Mauduit, A. Gransac, H., Auguste, P., Pillot, S., 2019. Study of AlSi7Mg0.6 Alloy by Selective Laser Melting: Mechanical Properties, Microstructure, Heat Treatment. Journal of Casting & Materials Engineering. 3, 1-13. https://doi.org/10.7494/jcme.2019.3.1.1

Moller, B., Schnabel, K., Wagener, R., Kaufmann, H., Melz, T., 2020. Fatigue assessment of additively manufactured AlSi10Mg laser beam welded to rolled EN AW-6082-T6 sheet metal. Journal of Fatigue. 140,105805. https://doi.org/10.1016/j.ijfatigue.2020.105805

Murali, S., Raman, K.S., Murthy, K.S.S., 1992. Effect of magnesium, iron (impurity) and solidification rates on the fracture toughness of Al7Si0.3Mg casting alloy. Materials Science and Engineering: A. 151, 1-10. https://doi.org/10.1016/0921-5093(92)90175-Z

Nahmany, M., Stern, A., Aghion, E., Frange, N., 2017. Structural Properties of EB-Welded $AlSi_{10}Mg$ Thin-Walled Pressure Vessels Produced by AM-SLM technology. Journal of Materials and Engineering Performance. 26,4813-4821. https://doi.org/10.1007/s11665-017-2953-7

Norris, J.T., Robino, C.V., Hirschfeld, D.A., Perricone, M.J., 2011. Effects of laser parameters on porosity formation: Investigating millimeter scale continuous wave Nd:YAG laser welds. Welding Journal. 17(6),431-437.

Oliveira de Menezes, J. T., Castrodeza, E. M., Casati, R., 2019. Effect of build orientation on fracture and tensile behavior of A357 Al alloy processed by Selective Laser Melting. Materials Science and Engineering: A. 766, 138392. https://doi.org/10.1016/j.msea.2019.138392

Pakdil, M., Çam, G., Koçak, M., Erim, S., 2011. Microstructural and mechanical characterization of laser beam welded AA6056 Al-alloy. Materials Science and Engineering. 528,7350-7356.

Pereira, J.C. et al., 2020. Comparison of AlSi7Mg0.6 alloy obtained by selective laser melting and investment casting processes: Microstructure and mechanical properties in as-built/as-cast and heat-treated conditions. Materials Science and Engineering A. 778, 139124. https://doi.org/10.1016/j.msea.2011.06.010

Prashanth, K.G., Damodaram, R., Maity, T., Wang, P., Eckert, J.,2017. Friction welding of selective laser melted Ti6Al4V parts. Materials science and engineering. 704,66-71. https://doi.org/10.1016/j.msea.2017.08.004

Rao, J. H., Zhang, Y., Fang, X., Chen, Y., Wu, X., Davies, C. H. J., 2017. The origins for tensile properties of selective laser melted aluminium alloy A357. Additive Manufacturing. 17, 113-122. https://doi.org/10.1016/j.addma.2017.08.007

Saariluoma, H., Piiroinen, A., Unt, A., Hakanen, J., Rautava, T., Salminen, A., 2020. Overview of Optical Digital Measuring Challenges and Technologies in Laser Welded Components in EV Battery Module Design and Manufacturing. Batteries. 6, 47. https://doi.org/10.3390/batteries6030047

Sánchez-Amaya, González-Rovira, L., Botana, F.J., 2009. Laser welding of aluminium alloys 5083 and 6082 under conduction regime. Applied Surface Science. 255, 9512-9521. https://doi.org/10.1016/j.apsusc.2009.07.081

Tan, C., Wang, D., Ma, W., Chen, Y., Chen, S., Yang, Y., Zhou, K., 2020. Design and additive manufacturing of novel conformal cooling molds. Materials & Design. 196, 109147. https://doi.org/10.1016/j.matdes.2020.109147

Tonelli, L., Liverani, E., Valli, G., Fortunato, A., Ceschini, L., 2020. Effects of powders and process parameters on density and hardness of A357 aluminum alloy fabricated by selective laser melting. The International Journal of Advanced Manufacturing Technology. 106, 371–383. https://doi.org/10.1007/s00170-019-04641-x

Tonelli, L., Liverani, E., Morri, A., Ceschini, L., 2021. Role of direct aging and solution treatment on hardness, microstructure and residual stress of the A357 (AlSi7Mg0.6) alloy produced by powder bed fusion. Metallurgical and Materials Transactions B. https://doi.org/10.1007/s11663-021-02179-6

Vilaro, T., Abed, S., Knapp, W., 2008. Direct manufacturing of technical parts using selective laser melting: example of automotive application. Proc. of 12th European Forum on Rapid Prototyping, March 5-6, 2008, Paris, France.

Xu J., Rong Y., Huang Y., Wang P., Wang C, 2018. Key-hole induced porosity formation during laser welding. Journal of Materials Processing Technology.252, 720-727. https://doi.org/10.1016/j.jmatprotec.2017.10.038

Yang, J. et al., 2019. Weldability, microstructure and mechanical properties of laser-welded selective laser melted 304 stainless steel joints. Journal of Material Science & technology. 35,1817-1824. https://doi.org/10.1016/j.jmst.2019.04.017

Yang, K.V., Rometsch, P., Davies, C.H.J., Huang, A., Wu, X., 2018. Effect of heat treatment on microstructure and anisotropy in mechanical properties of A357 alloy produced by selective laser melting. Materials & Design. 154, 275-290. https://doi.org/10.1016/j.matdes.2018.05.026

Zwicker, M.F.R., Moghadam, M., Zhang, W., Nielsen, C.V., 2020. Automotive battery pack manufacturing – a review of battery to tab joining. Journal of advanced Joining processes. 1, 100017. https://doi.org/10.1016/j.jajp.2020.100017